Title

The Functional Nanopore (FuN) Screen: A Versatile Genetic Assay to Study and Engineer Protein Nanopores in *Escherichia coli*

Authors

Wadim Weber[1,2], Markus Roeder[1], Helal Abujubara[3], Heinz Koeppl[1,4], Alesia Tietze[3] and Viktor Stein[1,2,*]

Affiliation

[1] Department of Biology, TU Darmstadt, 64287 Darmstadt, Germany

[2] Centre for Synthetic Biology, TU Darmstadt, 64283 Darmstadt, Germany

[3] Wallenberg Centre, University of Gothenburg, 41296 Gothenburg, Sweden

[4] Department of Electrical Engineering and Information Technology, TU Darmstadt, 64283 Darmstadt, Germany

*Correspondence should be addressed to Viktor Stein, Tel. +49 6151 16 21947; Fax. +49 6151 16 22063; Email: stein@bio.tu-darmstadt.de

Abstract

Nanopores comprise a versatile class of membrane proteins that carry out a range of key physiological functions and are increasingly exploited in many biotechnological applications. Yet, a capacity to study and engineer nanopores in the context of live cells has so far been hampered by a lack of suitable assays that provide sufficient experimental resolution and throughput. Addressing this technological gap, a newly developed Functional Nanopore (FuN) Screen now provides a highly quantitative read-out of nanopore function in *E. coli*. The assay is based on genetically-encoded fluorescent protein (FP) sensors that resolve the nanopore-dependent influx of Ca^{2+} across the inner membrane of *E. coli*. The FuN Screen is subsequently applied to dissect the molecular features that underlie the formation of nanopores by the $S^{21}68$ holin. This membrane peptide plays a critical role in the S^{21} bacteriophage life cycle as it assembles into defined nm-sized nanopores to initiate lysis of the host cell. Genetic mapping experiments complemented with high-resolution electrical recordings shedding detailed light on the molecular determinants that underlie the formation of $S^{21}68$ nanopores in the inner membrane. Overall, the FuN Screen is anticipated to facilitate both fundamental studies of nanopore functions and the construction of nanopores with tailored properties and function in *E. coli*.

Introduction

Nanopores comprise a versatile class of membrane proteins that form aqueous channels across cellular membranes and thus facilitate the passage of polar and charged molecules across an otherwise impermeable barrier. As part of their natural function, nanopores mediate important physiological functions such as cell lysis[1] or the permeation of antibiotics[2]. Recent years also witnessed the development of nanopores for different biotechnological applications[3], most prominently in the context of biosensing[4], DNA sequencing[4] and single molecule studies[5]. Notable nanopore scaffolds include oligomeric toxins such as αHLA[6–8], MspA[9], FraC[10,11] and ClyA[12], bacterial outer membrane proteins such as FhuA[13–15] and OmpG[16,17] and several self-assembling membrane peptides[18–21].

With a number of scaffolds emerging that can be used to engineer nanopores, their functional characterisation remains technically challenging, and has primarily been limited to electrophysiological methods in reconstituted lipid bilayers[22]. Highly preferable are genetic screening and selection systems that provide a quantitative and time-resolved read-out of nanopore function and are readily scalable in terms of throughput. Yet, progress in this regard has been hampered for several reasons: Firstly, considering their propensity to form aqueous channels, nanopores are toxic and therefore cannot be easily expressed in recombinant hosts. In addition, nanopores frequently comprise large, integral membrane proteins that rely on lipid environments for their functional expression and may require additional accessory factors to efficiently insert into cellular membranes.

Otherwise, in a few limited instances, genetic screening and selection systems such as liposome display[8] or a haemolytic assay[12] have been limited by technically challenging protocols that either rely on artificial cell-like compartments generated by means of *in vitro* compartmentalisation, or require expensive reagents such as red blood cells to assay nanopore functions on specialised target membranes. The latter has also been limited to bacterial toxins that rely on positive target membranes while reconstituted systems do not fully recapitulate important functional properties such as membrane potential[8].

Addressing this technological gap, a functional nanopore (FuN) assay now provides a facile, quantitative and time-resolved read-out of nanopore function in genetically-tractable *Escherichia coli*. Following experimental validation, the FuN screen is applied to dissect the key functional properties that underlie nanopore formation by the S^{21}68 holin[23]. Notably, the FuN Screen is able to resolve dynamic properties of nanopore functions in an *in vivo* context. Overall, the FuN Screen is anticipated to enable both complex engineering endeavours and foundational studies that aim to dissect the genetic and molecular features that underlie the functional properties of nanopores.

Materials and Methods

General Recombinant DNA Work

The DNA coding for the G-GECO fluorescent sensors, different nanopores incl. ion channels and thereof derived libraries was either purchased from public repositories (Addgene) or commercially synthesized as ssDNA (Sigma-Aldrich) or gBlocks (IDT DNA Technologies). DNA constructs for the expression of FP sensors and different nanopores were typically generated by means of conventional restriction-digestion-ligation cloning, Gibson Assembly[24] or iFLinkC[25]. Expression constructs were generally based on the pPro24[26,27] and the pCtrl2 backbones which was developed from pACYCT2[28]. Constructs were generally cloned in conventional DH10B (New England Biolabs) cloning strains before being transformed, expressed and assayed in BL21 (DE3) (New England Biolabs).

The FuN Screen Assay Principle

The nanopore and the FP sensor were expressed under the control of IPTG and propionate-inducible promoters from two separate expression plasmids that have been derived from the pPro24 and pCtrl2 backbones. Briefly, plasmids coding for the G-GECO[29] reporter and the nanopore of interest were co-transformed into BL21 (DE3) cells and plated on LB agar plates supplemented with 100 µg/mL ampicillin (AMP) and 25 µg/mL chloramphenicol (CHL).

For spectroscopic screening, individual colonies were used to inoculate 300 µL lysogeny broth (LB) medium supplemented with 100 µg/mL AMP and 25 µg mg/mL CHL and grown overnight in 96 deep-well plates at 37 ˚C and 1300 rpm. The following day 3.5 µL cell suspension was added to 196.5 µL LB supplemented with 25 mM sodium propionate pH 8.0, 100 µg/mL AMP and 25 µg/mL CHL in 96-well black microtitre plates with transparent bottom. Plates were incubated in a spectroscopic microtiter plate reader (TECAN Spark) at 30 ˚C with fluorescence and OD_{600} measurement every 3 minutes while being shaken at 180 rpm. Following 110 min of incubation, nanopore expression was initiated by adding 0.5 mM IPTG. The development of the fluorescent signal was measured through Ex. 480 ± 10 nm and Em. 525 ± 10 nm (Gain 60) along with the OD_{600} to assess cellular integrity. For quantitative analysis, the developing fluorescent signal was fit to **Eq. 1** through non-linear regression.

Eq. 1

$$f(x) = \boldsymbol{Bottom} + \frac{\boldsymbol{Top}}{1+e^{\frac{-(x-T_{1/2})}{\boldsymbol{Slope}}}}$$

For EDTA quench experiments, 5 mM EDTA was added approximately 15 min after the fluorescent signal saturated and cells stopped to divide as judged by the OD_{600}. The decreasing fluorescent signal was then measured through Ex. 480 ± 10 nm and Em. 525 ± 10 nm (Gain 60). The time point at which the fluorescent signal reached the basal level was then used to assess the stability of the nanopore.

For microfluidic analysis, individual colonies were used to inoculate 2 mL lysogeny broth (LB) supplemented with 100 µg/mL AMP and 25 µg mg/mL CHL and grown overnight in culture tubes at 37 ˚C and 180 rpm. The following day, 200 µL of this overnight suspension was used to inoculate 10 mL LB supplemented with 100 µg/mL AMP and 25 µg mg/mL CHL, and grown for 2 hours at 37 °C and 180 rpm. The cells were then centrifuged at 11,000 × g for 1 min and washed once with fresh LB medium. After a second centrifugation step at 11,000 × g for 1 min cells were resuspended in 100 µL sterile filtered LB supplemented with 100 µg/mL AMP and 25 µg mg/mL CHL. This suspension was used to seed a microfluidic chamber (manufactured by Wunderlichips GmbH, Zürich, Switzerland). Cells were grown at 37 °C and a flow rate of 4 µL/min controlled by a Flow EZ device (Fluigent) until a sufficient cell count was reached. The LB medium supplemented with 100 µg/mL AMP and 25 µg mg/mL CHL was then changed to LB medium supplemented with 100 µg/mL AMP, 25 µg mg/mL CHL and 25 mM sodium propionate pH 8.0 to induce the G-GECO1 expression at 30 °C and a flow rate of 4 µL/min. After 110 minutes, the medium was changed again to LB medium supplemented with 100 µg/mL AMP, 25 µg mg/mL CHL, 25 mM sodium propionate and 0.5 mM IPTG to induce nanopore expression. The developing fluorescent signal was monitored by means of a wide-field fluorescence microscope with a 480 ± 5 nm ex. laser (Huebner GmbH) with appropriate filters F58-019 (Dichroic Mirror) and em. F57-019 GFP/mCherry Dualband filter (AHF Analysentechnik. The design of the microfluidic incubation chamber for cultivating *E. coli* was adopted from previous studies[30].

Chemical Synthesis of $S^{21}68$ Holin Variants

The S^{21} holin variants, $S^{21}68$, $S^{21}10$-68, $S^{21}24$-68 und $S^{21}30$-38 peptides were synthesized on an INTAVIS MultiPep CF peptide synthesizer using a standard Fmoc-SPPS protocol on TentaGel® rink amide resin with a loading capacity of 0.21 mmol/g and *N,N,N′,N′*-tetramethyl-*O*-(1*H*-benzotriazol-1-yl)uronium hexafluorophosphate (HBTU, 5 equivalents relative to loading capacity) as a coupling reagent. The base 4-Methylmorpholine (NMM) in DMF was used in 2-fold excess to amino acids and coupling reagent. Each amino acid was attached by double coupling each 45 min at 60°C. The Fmoc- group deprotection was carried out twice by 20% piperidine in DMF. All coupling and Fmoc-deprotection steps were followed by intensive washing of the resin with DMF and dichloromethane. For the $S^{21}68$ peptide, four

pseudoprolines were inserted as described earlier.[31] At positions 15-16; 40-41 Gly-Ser(Psi(Me,Me)pro)-OH, at position 50-51 Leu-Thr(Psi(Me,Me)pro)-OH, at position 28-29 Val-Ser(Psi(Me,Me)pro)-OH and at position 4-5 Ile-Ser(Psi(Me,Me)pro)-OH were inserted.

Furthermore, co-solvent N-methylpyrrolidone (NMP) (10% v/v) was added to the coupling mixture and capping by 5% acetic anhydride (Ac_2O) in DMF was performed after every 10th coupling cycle. All peptides were cleaved from the resin as described previously.[32]

Peptides were purified by high-performance liquid chromatography (RP-HPLC) employing a Waters 1525 binary pump and a Waters 2998 PDA detector on a customized Waters 600 module equipped with a Waters 996 PDA detector (Waters, Milford, MA, USA). The gradient elution system was 0.1% trifluoracetic acid (TFA) in water (eluent A) and 0.1% TFA in acetonitrile (eluent B). The peptides S^{21}10-68, S^{21}24-68 und S^{21}30-68 were eluted on a MultoKrom® 100-5 C18 column (250 x 20 mm) column with a linear gradient of 25-60% eluent B for 10 min followed by gradient 60-80% eluent B for 60 min with a flow rate of 8 mL/min. Peptide S^{21}68 was eluted on a MultoHighBio® 100-5 C4 column (250 x 20 mm) with a linear gradient of 40-90% eluent B in 120min with a flow rate of 8 mL/min. The peaks were detected at 214 nm. Collected fractions were combined, freeze-dried and stored at -28°C.

The purity of the collected fractions was confirmed by analytical RP-HPLC on a Waters XC e2695 system (Waters, Milford, MA, USA) employing a Waters PDA 2998 diode array detector equipped with an ISERA® C18 (50 x 4.6 mm, 5.0 µm) column. Peptides S^{21}10-68, S^{21}24-68 und S^{21}30-68 were eluted with a gradient of 50% - 90% eluent B in 10 min at a flow rate of 2 mL/min (detection at 214 nm). For peptide S^{21}68, Vydac® C4 (150 x 4.6 mm, 5µm) column was used, with a gradient of 40−90% eluent B over 30 min at flow rate of 1 mL/min (detection at 214 nm). The molecular weight of the purified peptides was confirmed by ESI mass on a Waters Synapt G2-Si ESI mass spectrometer equipped with a Waters Acquity UPLC system.

Electrophysiological Characterisation of S^{21} Holin Variants

The pore-forming properties of wildtype S^{21}68 and thereof derived holin variants S^{21}10-68, S^{21}24-68, and S^{21}30-68 were functionally characterised in a vertical bilayer set up at room temperature as previously described[33]. Chambers were connected with Ag/AgCl electrodes to the head-stage of a patch clamp amplifier L/M-EPC-7 (List-Medical). Applied membrane potentials were referenced to the *cis* compartment. Current traces were filtered at 1 kHz and digitized with a sampling frequency of 5 kHz by an A/D-converter LIH 1600 (HEKA Elektronik). Both chambers were filled with 100 mM KCl 10 mM HEPES pH 7.0 and 1,2-diphytanoyl-sn-glycero-3-phosphocholine (DPhPC) bilayers were formed by air bubble technique[33]. Nanopore peptides were dissolved in DMSO with a concentration of 100 mg/mL and stored up to 3 weeks at 4°C. For bilayer measurements 1 µL of the stock solution was diluted in 1000 µL 100 mM

KCl 10 mM HEPES pH 7.0 and 5-10 µL were added directly above the bilayer in the *trans* compartment with a Hamilton syringe. Following successful insertion and assembly of nanopore several rounds of a voltage protocol were applied with 100 mV for 5 sec followed by -100 mV for 5 sec.

Results

A Genetic Reporter Assay to Screen for Nanopore Function in High-Throughput

To assay protein nanopore function in high-throughput, a reporter-based genetic screening system was developed (**Fig. 1**). Briefly, the assay relies on genetically-encoded Ca^{2+} indicators for optical imaging (GECOs)[29] to resolve the nanopore-dependent influx of Ca^{2+} into the cytoplasm of *E. coli* and thus provides a time-resolved optical read-out of nanopore function. To minimise delays in the signal associated with the maturation of the fluorophore, the assay was established with the green fluorescent G-GECO[29]. To ensure independent control over the expression of the reporter and the nanopore, transcriptional units were placed on separate plasmids with compatible origins of replications while their transcription was initiated with *E. coli* and T7 RNA polymerases under the control of propionate and IPTG-inducible promoters.

Validation of the FuN Screen Assay Principle

Once a set of expression constructs was established, the FuN Screen was experimentally validated. In particular, it was examined whether the fluorescent signal associated with a Ca^{2+}-dependent influx is specific to the functional properties of distinct nanopores and ion channels. To this end, the $S^{21}68$ holin[23], the T4 holin[34] and the K_{CV}NTS channel[35,36] served as model nanopores and ion channels. Briefly, the T4 holin and the $S^{21}68$ holin both derive from bacteriophages where they initiate cell lysis by forming nm- to µm-sized pores in the inner membrane of *E. coli*[37]. In contrast, the K_{CV}NTS channel derives from Chlorella virus and exerts a high selectivity for K^+ ions and thus provides a suitable negative control. To afford a quantitative measure of nanopore function, the resultant fluorescent signal was empirically fit to **Eq. 1** where the slope and the time $T_{½}$ required to reach half the signal provide a measure for nanopore formation (**Fig. 2**). In addition, the OD_{600} was monitored as an independent parameter to assess cellular integrity following expression of a nanopore.

Crucially, the expression of $S^{21}68$ and the T4 holin triggered a strong increase in the fluorescent signal while the K^+-selective K_{CV}NTS channel did not (**Fig. 2**). In addition, the fluorescent signal can be readily reversed by adding EDTA which triggers a rapid drop in the signal for both the T4 holin and $S^{21}68$ (**Fig. 2**). Differences were however observed in terms

of the OD_{600} which dropped sharply for the T4 holin but declined more gradually for $S^{21}68$. These differences can be attributed to different effects on cellular integrity as the T4 holin forms large µm-sized holes that cause a cell to disintegrate[38] in contrast to $S^{21}68$ which forms smaller and defined nm-sized pores leaving the cell intact for a prolonged period of time[39].

To examine how the expression of a functional nanopore affects the structural integrity of the cell and how it correlates with the developing fluorescent signal, the expression of individual nanopores was examined by fluorescence microscopy at single cell resolution in a microfluidic incubation chamber (**Fig. 3**). In all cases, cells rapidly stopped to divide while the fluorescent signal averaged across the incubation chamber generally matched the course of the fluorescent signal observed by fluorescence spectroscopy in microtitre plates (**Fig. 2**). Notably, the expression of the T4 holin and $S^{21}68$ triggered a strong early increase in the fluorescent signal within 80-100 min before gradually fading in the case of $S^{21}68$ (as a result of bleaching). In terms of the structural integrity of the cell-envelope, cellular structures disappear for the T4 holin as it forms µm-sized holes that trigger cell lysis and enable the G-GECO to diffuse out of the cell. In contrast, cellular structures remain visible and intact for prolonged periods of time in case of $S^{21}68$ and K_{CV}NTS. Furthermore, only a very late increase in the fluorescent signal was observed for K_{CV}NTS at 380 min as membrane homeostasis eventually breaks down leading to an influx of Ca^{2+} into the cell.

Dissecting $S^{21}68$ Nanopore Activation

With an elementary fluorescence-based assay established, the FuN Screen was applied to dissect the molecular features that underlie the formation of $S^{21}68$ nanopores (**Fig. 4**). The current mechanism hypothesises that $S^{21}68$ along with its cognate anti-holin $S^{21}71$, which features an additional three amino acid cytoplasmic anchor at its N-terminus, initially accumulate as inactive, anti-parallel α-helical heterodimers in the inner membrane of *E. coli*[40]. Upon reaching a critical concentration, the N-terminal transmembrane domain, termed TMD1, flips across the inner membrane to initiate the assembly of heptameric nanopores[23] (**Fig. 4B**). Yet, little is known which molecular features control the translocation of TMD1 across the inner membrane and subsequently mediate the stability of the $S^{21}68$ nanopore.

Thus, to gain a more quantitative understanding of the molecular features underlying the formation of $S^{21}68$ nanopores while demonstrating the exquisite quantitative and temporal resolution of the FuN Screen, the two most N-terminal residues D2 and K3 were substituted with 17 different amino acids and their effect on the formation of $S^{21}68$ nanopores quantified in terms of $T_{½}$ (**Fig. 5A** and **Fig. 5B**). Note, Met and Cys were omitted to prevent artefacts that may arise through an alternative start codon and the formation of disulphide bridges in the periplasm. Substitutions generally had a greater effect on K3 relative to D2. Furthermore, the

results could be rationalised with empiric rules previously defined for the folding of membrane proteins[41,42]. This means, all substitutions in K3 except for Arg significantly accelerated the formation of $S^{21}68$ nanopores. This suggests that positively charged side chains anchor the N-terminus in the cytoplasm *via* electrostatic interactions with the negatively charged head groups of the phosphate lipids[43] and thus delay translocation of TMD1 across the inner membrane. Conversely, hydrophobic and negatively charged side chains assisted by the membrane potential facilitate the translocation of TMD1 across the membrane. In comparison, substitution of D2 generally had a lesser effect on the propensity of $S^{21}68$ to form nanopores. This means, hydrophobic amino acids Ile, Leu and Phe slightly accelerated nanopore formation while polar residues slowed the formation of $S^{21}68$ nanopores upon removal of the native D2 negative charge, which drives translocation assisted by the negative membrane potential. Similar phenomena were previously observed in the folding of membrane and defined as the 'positive-inside' and 'negative-outside' rules[41].

To dissect the capacity of individual mutants to insert, activate and form stable nanopores, the functional properties of $S^{21}68$ nanopores were analysed by means of EDTA quench experiments following saturation of the fluorescent signal when cells stopped to divide and no further nanopores were expressed. Considering nanopores have already formed at this stage, the fluorescent signal becomes independent of insertion and activation, but primarily depends on the functional properties of assembled nanopores in the membrane. Again, striking differences were observed for substitutions in K3 (**Fig. 5D** and **Fig. 5F**) but not D2 (**Fig. 5C** and **Fig. 5E**). This time however, the ability to quench the fluorescent signal by EDTA strongly correlated with hydrophilic/hydrophobic nature of the amino acid side chains (**Fig. 5D** and **Fig. 5F**). This means, hydrophilic residues were generally comparable to K3 as the fluorescent signal was rapidly quenched upon addition of EDTA. In contrast, hydrophobic substitutions showed a marked increase in the time required to quench the fluorescent signal implying that the resultant nanopores are less stable slowing down the effusion of Ca^{2+} out of the cell. Overall, these results highlight a dual role for K3 in the formation of $S^{21}68$ nanopores as it initially delays activation, but subsequently ensures stability.

Delineating Minimal Pore Forming Motifs of $S^{21}68$

In a second set of experiments, $S^{21}68$ was systematically truncated to identify the molecular features that are necessary and sufficient to form nanopores. To this end, TMD1 was truncated in increments of two amino acids and their propensity to form nanopores quantified in terms of $T_{½}$ (**Fig. 6A**). Notably, nanopore formation decreased upon removal of D2 (see $S^{21}2$-68) but was quickly regained following deletion of K3 and I4 (see $S^{21}4$-68). This result further confirmed the anchoring role of K3 that exerts an inhibitory effect that is partially offset by the

negative charge of D2. A very strong propensity to form nanopores was subsequently maintained until deletion of the aromatic, hydrophobic patch YWFLQW (see S^{21}24-68) and partially regained following removal of the hydrophilic LDQVSPSQ loop connecting TMD1 with TMD2 (see S^{21}30-68). This could either arise through a decelerated formation of S^{21}68 nanopores or reduced stability.

To examine this aspect further, truncation mutants were subject to EDTA quench experiments to assess their propensity to form nanopores independent of expression, insertion and activation kinetics. Notably, once K3 was deleted, truncation mutants formed less stable nanopores as judged by decreased quench rates upon addition of EDTA (**Fig. 6A** and **Fig. 6C**). This suggests that the enhanced ability of truncation mutants to form nanopores as judged by the $T_{½}$ is primarily enabled by a better ability of the N-terminus to translocate across the membrane while the actual pores turn out less stable. This becomes particularly obvious when comparing the course of the fluorescent signal for S^{21}68 and S^{21}2-68 with S^{21}24-68 and S^{21}30-68 which display comparable $T_{½}$, but different EDTA quench rates.

Electrophysiological Characterisation of Minimal S^{21}68 Holin Motifs

To gain a more quantitative understanding of N-terminal truncations and verify observations made in the FuN Screen using a complementary experimental technique, four representative truncations S^{21}68, S^{21}10-68, S^{21}24-68, and S^{21}30-68 were chemically synthesized and electrophysiologically characterised in reconstituted vertical lipid bilayer membranes *in vitro* (**Fig. 7A**). Notably, electrical recordings demonstrate a good correlation with the fluorescent signal observed in the FuN screen highlighting its physiological relevance. This means, judging by the average conductivity, S^{21}10-68 displayed the strongest propensity to insert and assemble into functional nanopores (**Fig. 7B**). Furthermore, distinct functional states can be observed for S^{21}68, S^{21}10-68 and S^{21}24-68 (**Fig. 7A**). In contrast, the shortest truncation S^{21}30-68 only displayed poorly defined pores with characteristic spikes reflecting the transient nature of the nanopores**.** Overall, these results confirm that TMD2 of S^{21}68 is necessary and sufficient to form nanopores albeit very transient ones while the very N-terminus of S^{21}68 determines its stability as judged by the duration and number of distinct conductive states.

Discussion

Nanopores comprise a versatile class of membrane proteins that carry out a range of key physiological functions and are increasingly exploited for different biotechnological applications. Yet, the limited capacity to assay nanopores in the context of live cells in a quantitative and time-resolved fashion has so far hampered both fundamental studies to understand the molecular and genetic features that underlie the functional properties of nanopores and more sophisticated engineering endeavours.

Addressing this technological gap, nanopores can now be studied and engineered by means of the FuN Screen. The assay relies on the nanopore-dependent influx of Ca^{2+} that is resolved with genetically-encoded Ca^{2+}-specific FP sensors. Crucially, the assay recapitulates the functional properties of different nanopores and ion channels as it is specific for Ca^{2+} while the K^+ permeable K_{CV}NTS channel does not generate a fluorescent signal. Furthermore, the FuN Screen carries a number of unique and advantageous feature. First of all, its read-out is compatible with different optical read-outs, for instance, based on fluorescence spectroscopy in microtitre plates for medium throughput, or fluorescence microscopy in a microfluidic incubation chamber for high-resolution studies at single cell level. Secondly, all components are genetically-encoded and therefore do not rely on external reagents. Thirdly, experimental protocols are simple and can be readily realised in any molecular biology lab. Finally, the FuN Screen is highly quantitative and capable of resolving the dynamic properties underlying the formation of nanopores in the context of *E. coli*.

The capacity of the FuN Screen is demonstrated by dissecting the molecular features that underlie the insertion, activation and stability of $S^{21}68$ nanopores. In this regard, early genetic and recent biophysical studies hypothesized that TMD2 is necessary and sufficient to form functional nanopores while the N-terminal affects the efficiency of activation[44–48]. Truncation experiments by means of the FuN Screen complemented by electrophysiological characterisation of chemically synthesized peptides confirm that TMD2 is necessary and sufficient to form nanopores in the inner membrane of *E. coli* albeit very transient ones. This means, portions of TMD1 and particularly the very N-terminus of TMD1 confer stability. Notably, systematic truncation and randomisation of the $S^{21}68$ N-terminus unveil a dual role for K3 regulating timing, but also the stability of $S^{21}68$ nanopores. Notably, both the deletion and substitution of K3 (with the exception of Arg) rapidly accelerate nanopore formation as it no longer anchors the N-terminus of TMD1 in the cytosol *via* electrostatic interactions with the charged phospholipid headgroups. At the same time, it positively contributes to the stability of $S^{21}68$ nanopores. Genetic data implies a need for the N-terminus to be hydrophilic possibly favouring solvation in the periplasm as hydrophobic residues result in less stable nanopores.

Acknowledgments

The authors acknowledge support by Christine Pleitner and Theresa Wörmann assisting with experimental efforts and Gerhard Thiel for helpful comments and suggestions concerning the electrophysiological characterisation of the $S^{21}68$ holin and thereof derived variants.

Funding

LOEWE iNAPO, Hessen State Ministry of Higher Education, Research and the Arts (VS, AT); Pioneer ACTIVATOR (Project No. 527 00 962), TU Darmstadt (VS); The Knut and Alice Wallenberg Foundation via the Wallenberg Centre for Molecular and Translational Medicine (AT) and Swedish Research Council (2020-04299) (AT) are gratefully acknowledged.

References

1. Peraro, M. D. & Van Der Goot, F. G. Pore-forming toxins: Ancient, but never really out of fashion. *Nature Reviews Microbiology* (2016). doi:10.1038/nrmicro.2015.3
2. Vergalli, J. *et al.* Porins and small-molecule translocation across the outer membrane of Gram-negative bacteria. *Nature Reviews Microbiology* **18**, (2020).
3. Ayub, M. & Bayley, H. Engineered transmembrane pores. *Curr. Opin. Chem. Biol.* **34**, 117–126 (2016).
4. Wang, S., Zhao, Z., Haque, F. & Guo, P. Engineering of protein nanopores for sequencing, chemical or protein sensing and disease diagnosis. *Current Opinion in Biotechnology* (2018). doi:10.1016/j.copbio.2017.11.006
5. Movileanu, L. Interrogating single proteins through nanopores: challenges and opportunities. *Trends in Biotechnology* (2009). doi:10.1016/j.tibtech.2009.02.008
6. Gu, L. Q., Braha, O., Conlan, S., Cheley, S. & Bayley, H. Stochastic sensing of organic analytes by a pore-forming protein containing a molecular adapter. *Nature* (1999). doi:10.1038/19491
7. Braha, O. *et al.* Designed protein pores as components for biosensors. *Chem. Biol.* (1997). doi:10.1016/S1074-5521(97)90321-5
8. Fujii, S., Matsuura, T., Sunami, T., Kazuta, Y. & Yomo, T. In vitro evolution of α-hemolysin using a liposome display. *Proc. Natl. Acad. Sci. U. S. A.* **110**, 16796–801 (2013).
9. Derrington, I. M. *et al.* Nanopore DNA sequencing with MspA. *Proc. Natl. Acad. Sci. U. S. A.* (2010). doi:10.1073/pnas.1001831107
10. Wloka, C., Mutter, N. L., Soskine, M. & Maglia, G. Alpha-Helical Fragaceatoxin C Nanopore Engineered for Double-Stranded and Single-Stranded Nucleic Acid Analysis. *Angew. Chemie - Int. Ed.* **55**, 12494–12498 (2016).
11. Huang, G., Willems, K., Soskine, M., Wloka, C. & Maglia, G. Electro-osmotic capture and ionic discrimination of peptide and protein biomarkers with FraC nanopores. *Nat. Commun.* (2017). doi:10.1038/s41467-017-01006-4
12. Soskine, M., Biesemans, A., De Maeyer, M. & Maglia, G. Tuning the size and properties of ClyA nanopores assisted by directed evolution. *J. Am. Chem. Soc.* **135**, 13456–13463 (2013).

13. Thakur, A. K. & Movileanu, L. Real-time measurement of protein–protein interactions at single-molecule resolution using a biological nanopore. *Nat. Biotechnol.* (2019). doi:10.1038/nbt.4316
14. Thakur, A. K. & Movileanu, L. Single-molecule protein detection in a biofluid using a quantitative nanopore sensor. *ACS Sensors* (2019). doi:10.1021/acssensors.9b00848
15. Liu, Z., Ghai, I., Winterhalter, M. & Schwaneberg, U. Engineering Enhanced Pore Sizes Using FhuA Δ1-160 from E. coli Outer Membrane as Template. *ACS Sensors* (2017). doi:10.1021/acssensors.7b00481
16. Chen, M., Khalid, S., Sansom, M. S. P. & Bayley, H. Outer membrane protein G: Engineering a quiet pore for biosensing. *Proc. Natl. Acad. Sci. U. S. A.* (2008). doi:10.1073/pnas.0711561105
17. Sanganna Gari, R. R., Seelheim, P., Liang, B. & Tamm, L. K. Quiet Outer Membrane Protein G (OmpG) Nanopore for Biosensing. *ACS Sensors* (2019). doi:10.1021/acssensors.8b01645
18. Lella, M., Kamilla, S., Jain, V. & Mahalakshmi, R. Molecular Mechanism of Holin Transmembrane Domain i in Pore Formation and Bacterial Cell Death. *ACS Chem. Biol.* **11**, 910–920 (2016).
19. Krishnan, S. *et al.* Autonomously Assembled Synthetic Transmembrane Peptide Pore. *J. Am. Chem. Soc.* (2019). doi:10.1021/jacs.8b09973
20. Lella, M. & Mahalakshmi, R. Engineering a Transmembrane Nanopore Ion Channel from a Membrane Breaker Peptide. *J. Phys. Chem. Lett.* (2016). doi:10.1021/acs.jpclett.6b00987
21. Mahendran, K. R. *et al.* A monodisperse transmembrane α-helical peptide barrel. *Nat. Chem.* (2017). doi:10.1038/nchem.2647
22. Shen, H. H., Lithgow, T. & Martin, L. L. Reconstitution of membrane proteins into model membranes: Seeking better ways to retain protein activities. *International Journal of Molecular Sciences* (2013). doi:10.3390/ijms14011589
23. Park, T., Struck, D. K., Deaton, J. F. & Young, R. Topological dynamics of holins in programmed bacterial lysis. *Proc. Natl. Acad. Sci. U. S. A.* (2006). doi:10.1073/pnas.0600943103
24. Gibson, D. G. *et al.* Enzymatic assembly of DNA molecules up to several hundred kilobases. *Nat. Methods* **6**, 343–5 (2009).
25. Gräwe, A., Ranglack, J., Weyrich, A. & Stein, V. iFLinkC : an iterative functional linker cloning strategy for the combinatorial assembly and recombination of linker peptides with functional domains. *Nucleic Acids Res.* 1–11 (2020). doi:10.1093/nar/gkz1210
26. Lee, S. K. & Keasling, J. D. A propionate-inducible expression system for enteric bacteria. *Appl. Environ. Microbiol.* **71**, (2005).

27. Lee, S. K. & Keasling, J. D. Propionate-regulated high-yield protein production in Escherichia coli. *Biotechnol. Bioeng.* **93**, (2006).
28. Ponchon, L. *et al.* Co-expression of RNA-protein complexes in Escherichia coli and applications to RNA biology. *Nucleic Acids Res.* **41**, (2013).
29. Kalko, E. K. V *et al.* An Expanded Palette of Genetically Encoded Ca2+ Indicators. *Science (80-.).* **333**, 1888–1891 (2011).
30. Santos-Moreno, J., Tasiudi, E., Stelling, J. & Schaerli, Y. Multistable and dynamic CRISPRi-based synthetic circuits. *Nat. Commun.* (2020). doi:10.1038/s41467-020-16574-1
31. Mutter, M. & Vuilleumier, S. A Chemical Approach to Protein Design—Template-Assembled Synthetic Proteins (TASP). *Angewandte Chemie International Edition in English* **28**, (1989).
32. Baumruck, A. C., Tietze, D., Steinacker, L. K. & Tietze, A. A. Chemical synthesis of membrane proteins: A model study on the influenza virus B proton channel. *Chem. Sci.* **9**, (2018).
33. Braun, C. J., Baer, T., Moroni, A. & Thiel, G. Pseudo painting/air bubble technique for planar lipid bilayers. *J. Neurosci. Methods* **233**, (2014).
34. Ramanculov, E. & Young, R. Genetic analysis of the T4 holin: Timing and topology. *Gene* (2001). doi:10.1016/S0378-1119(01)00365-1
35. Braun, C. J. *et al.* Viral potassium channels as a robust model system for studies of membrane-protein interaction. *Biochim. Biophys. Acta - Biomembr.* **1838**, (2014).
36. Pagliuca, C. *et al.* Molecular properties of Kcv, a virus encoded K+ channel. *Biochemistry* **46**, (2007).
37. Reddy, B. L. & Saier, M. H. Topological and phylogenetic analyses of bacterial holin families and superfamilies. *Biochim. Biophys. Acta - Biomembr.* (2013). doi:10.1016/j.bbamem.2013.07.004
38. Tran, T. A. T., Struck, D. K. & Young, R. Periplasmic domains define holin-antiholin interactions in T4 lysis inhibition. *J. Bacteriol.* **187**, (2005).
39. Park, T., Struck, D. K., Dankenbring, C. A. & Young, R. The pinholin of lambdoid phage 21: Control of lysis by membrane depolarization. *J. Bacteriol.* **189**, (2007).
40. Young, R. Bacteriophage holins: Deadly diversity. in *Journal of Molecular Microbiology and Biotechnology* **4**, (2002).
41. Baker, J. A., Wong, W. C., Eisenhaber, B., Warwicker, J. & Eisenhaber, F. Charged residues next to transmembrane regions revisited: 'Positive-inside rule' is complemented by the 'negative inside depletion/outside enrichment rule'. *BMC Biol.* **15**, (2017).
42. von Heijne, G. The distribution of positively charged residues in bacterial inner

membrane proteins correlates with the trans-membrane topology. *EMBO J.* **5**, (1986).

43. Raetz, C. R. H. Enzymology, genetics, and regulation of membrane phospholipid synthesis in Escherichia coli. *Microbiol. Rev.* **42**, (1978).
44. Steger, L. M. E. *et al.* Structural and functional characterization of the pore-forming domain of pinholin S2168. *Proc. Natl. Acad. Sci. U. S. A.* **117**, (2020).
45. Ahammad, T. *et al.* Continuous Wave Electron Paramagnetic Resonance Spectroscopy Reveals the Structural Topology and Dynamic Properties of Active Pinholin S2168 in a Lipid Bilayer. *J. Phys. Chem. B* **123**, (2019).
46. Ahammad, T. *et al.* Structural Dynamics and Topology of the Inactive Form of S21Holin in a Lipid Bilayer Using Continuous-Wave Electron Paramagnetic Resonance Spectroscopy. *J. Phys. Chem. B* **124**, (2020).
47. Ahammad, T. *et al.* Conformational differences are observed for the active and inactive forms of pinholin S21 using deer spectroscopy. *J. Phys. Chem. B* **124**, (2020).
48. Pang, T., Fleming, T. C., Pogliano, K. & Young, R. Visualization of pinholin lesions in vivo. *Proc. Natl. Acad. Sci. U. S. A.* **110**, (2013).

Figures and Captions

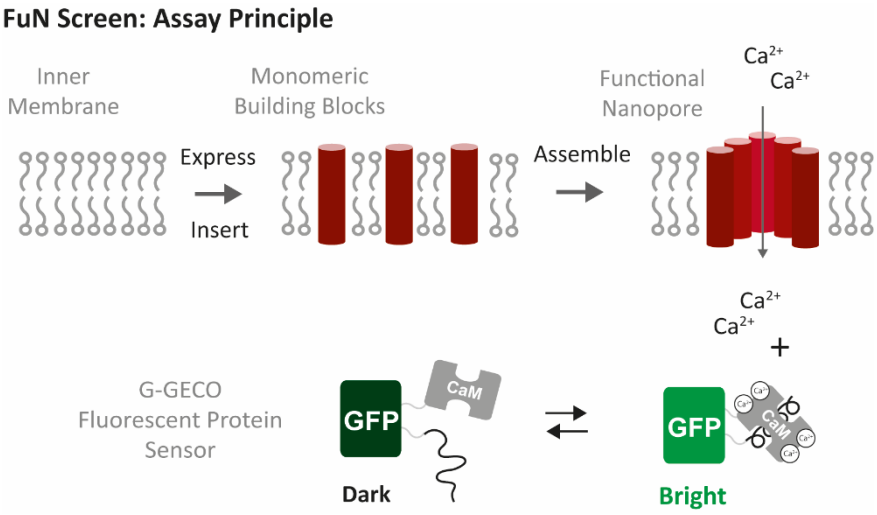

Fig. 1: Schematic overview of the FuN Screen assay principle. Following the expression of a nanopore in *E.coli* and its functional assembly, Ca^{2+} ions flow across the inner membrane into the cytoplasm. The influx of Ca^{2+} is experimentally resolved by G-GECOs and provides a quantitative and time-resolved fluorescent read-out of nanopore function in *E. coli*.

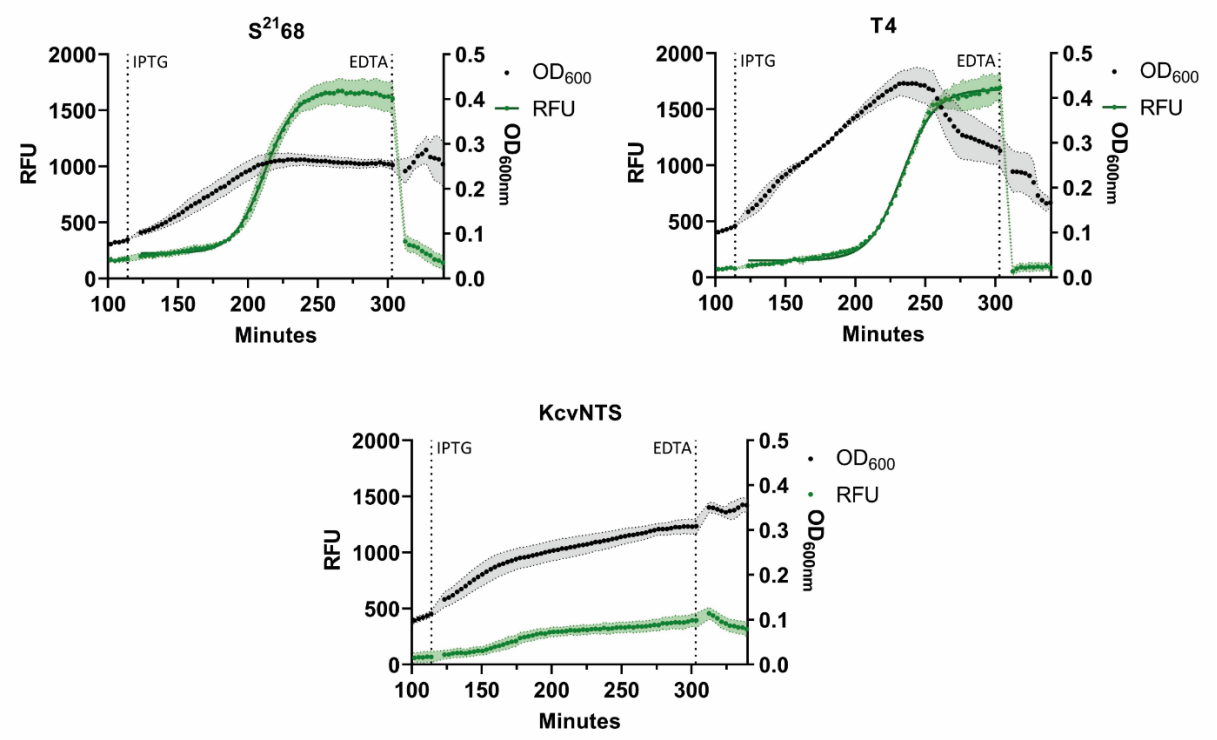

Fig. 2: Experimental validation of the FuN Screen by fluorescence spectroscopy in microtitre plates. The expression of different nanopores $S^{21}68$, T4 holin, and $K_{CV}NTS$ is induced with IPTG which subsequently triggers a strong increase in the fluorescent signal for $S^{21}68$ and the T4 holin, but not $K_{CV}NTS$ demonstrating that an influx of Ca^{2+} correlates with the functional properties of a nanopore. The fluorescent signal can be reversed by adding EDTA.

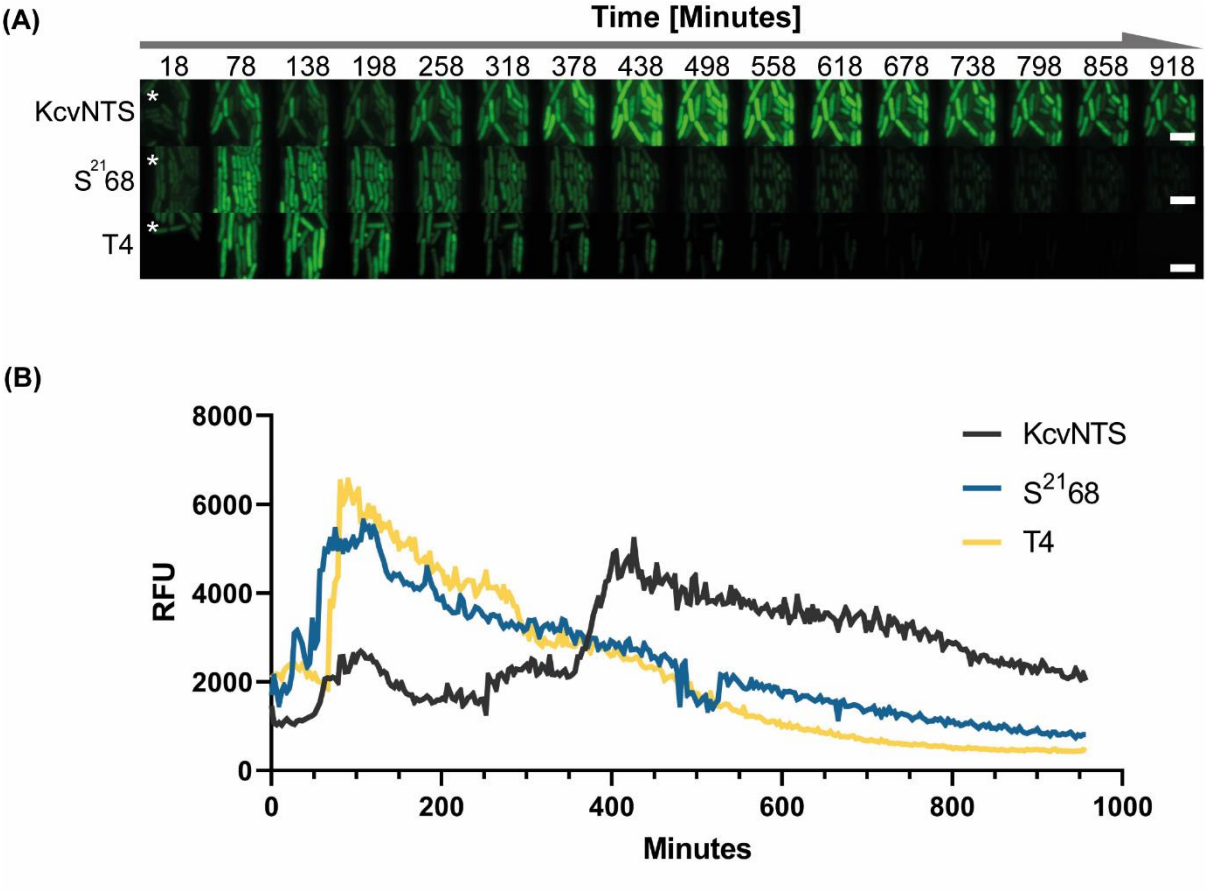

Fig. 3: Experimental validation of the FuN Screen assay principle by fluorescence microscopic measurements following incubation of cells in a microfluidic incubation chamber. **(A)** Correlating the developing fluorescent signal for $S^{21}68$ holin, the T4 holin and $K_{CV}NTS$ channel with cellular physiology at single cell resolution, which demonstrates that cellular integrity remains intact upon expression of $S^{21}68$ and the $K_{CV}NTS$ channel, but not the T4 holin; **(B)** Quantitative comparison of the developing fluorescent signal averaged across the microfluidic incubation chamber. In contrast to $K_{CV}NTS$, the expression of the $S^{21}68$ and the T4 holin trigger a rapid increase in the fluorescent signal demonstrating the functional specificity of the FuN Screen read-out.

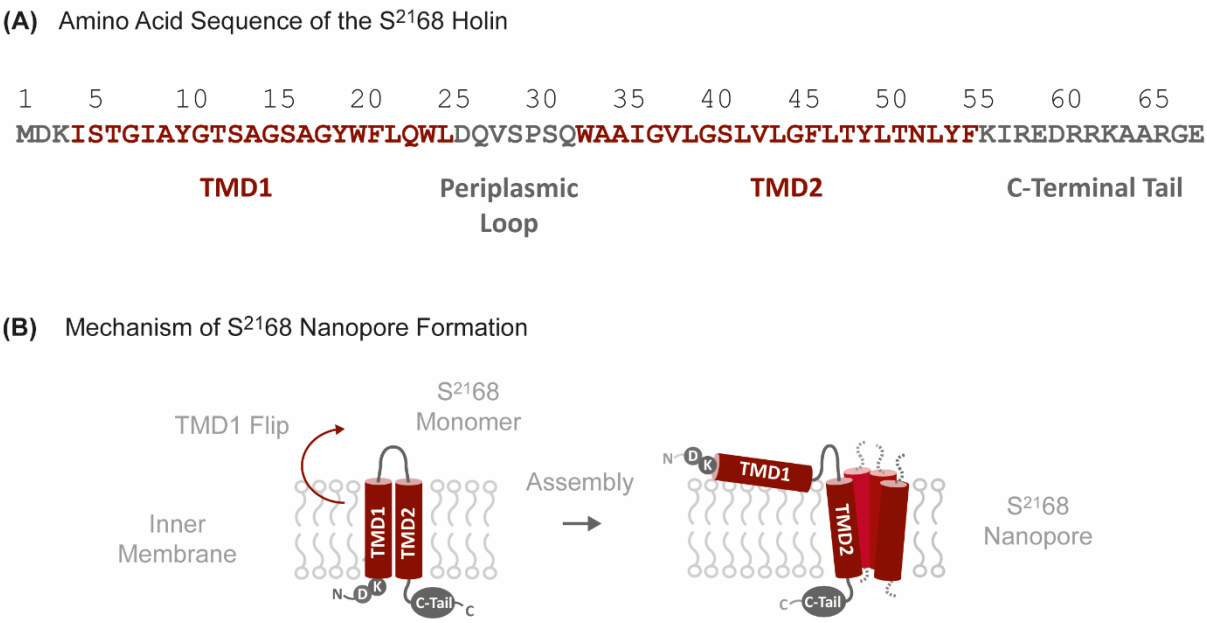

Fig. 4: Structural organisation of the S^{21}68 holin. **(A)** Primary structure of the S^{21}68 holin. Transmembrane regions are denoted in red while cytoplasmic and periplasmic regions are denoted in grey. **(B)** Simplified mechanism of nanopore formation by S^{21}68. Upon expression and reaching a critical concentration in the inner membrane, the N-terminal transmembrane domain (TMD1) flips across the inner membrane to initiate the assembly of defined heptameric nanopores stabilizing it in the membrane.

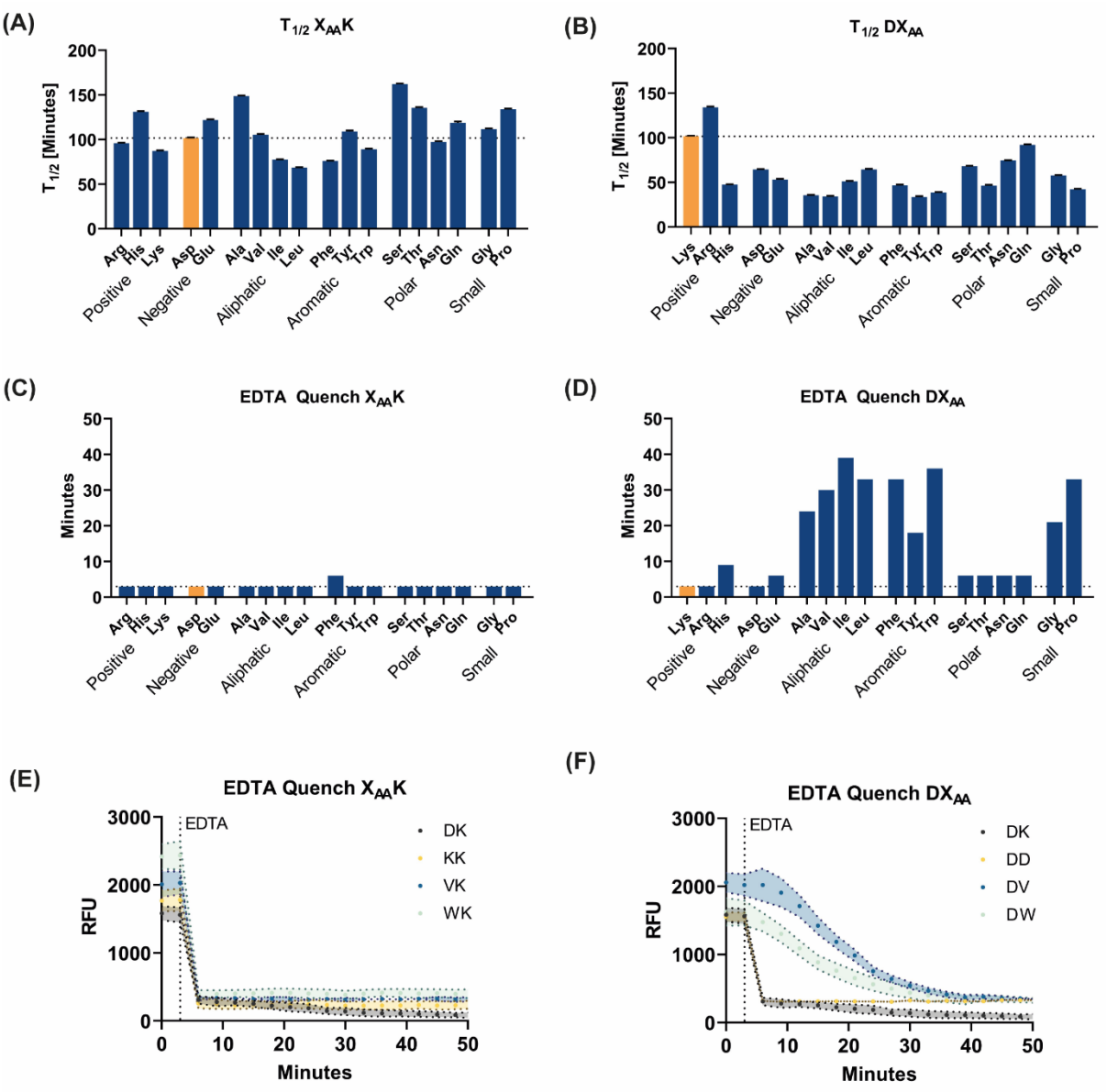

Fig. 5: Probing the contribution of N-terminal residues in the formation and stability of $S^{21}68$ nanopores. **(A, B)** Summary of $T_{½}$ for systematic substitutions of D2 and K3. Substitution of D2 is largely insensitive to mutations. In contrast, all substitutions of K3 except Arg lead to an acceleration of nanopore formation highlighting the role of positive charges which anchor the N-terminus in the cytoplasm and delay the formation of nanopores; **(C, D)** Summary of EDTA quench experiments for systematic substitutions of D2 and K3; D2 is largely insensitive to mutations. In contrast, hydrophilic substitutions of K3 maintain the stability of nanopore while hydrophobic substitutions form less stable nanopores as judged by prolonged EDTA quench rates. The time required to quench the fluorescent signal was defined as the time required for the fluorescent signal to drop to the base level (identified manually); **(E, F)** Representative kinetic traces of EDTA quench experiments. For the wild-type $S^{21}68$ as well D2 substitutions, the signal is quenched immediately upon addition of 5 mM EDTA while substitutions of K3 with Val and Trp prolonged the quenching time.

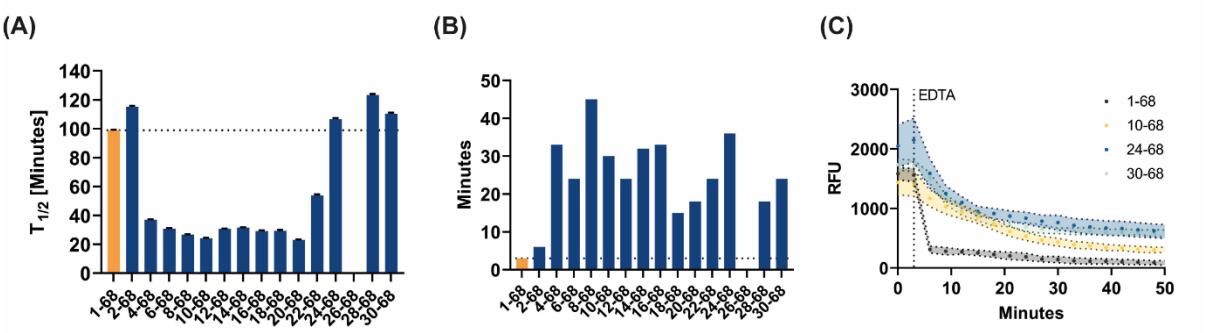

Fig. 6: Delineating the minimal pore-forming motif of $S^{21}68$. **(A)** Summary of $T_{½}$ for systematic N-terminal truncations. Following deletion of K3 the ability to form nanopores is enhanced before deletion of a hydrophobic patch starting with truncation mutant $S^{21}22$-68; **(B)** Summary of EDTA quench experiments for N-terminal truncations looking to assess the stability of truncation mutants independent of expression, insertion and activation kinetics. Following deletion of K3, truncation mutants are destabilised as judged by a prolonged time to quench the fluorescent signal upon addition of EDTA; The time required to quench the fluorescent signal was defined as the time required for the fluorescent signal to drop to the base level (identified manually); **(C)** Representative kinetic traces of EDTA quench experiments. For the wild-type $S^{21}68$ the signal is quenched immediately upon addition of 5 mM EDTA.

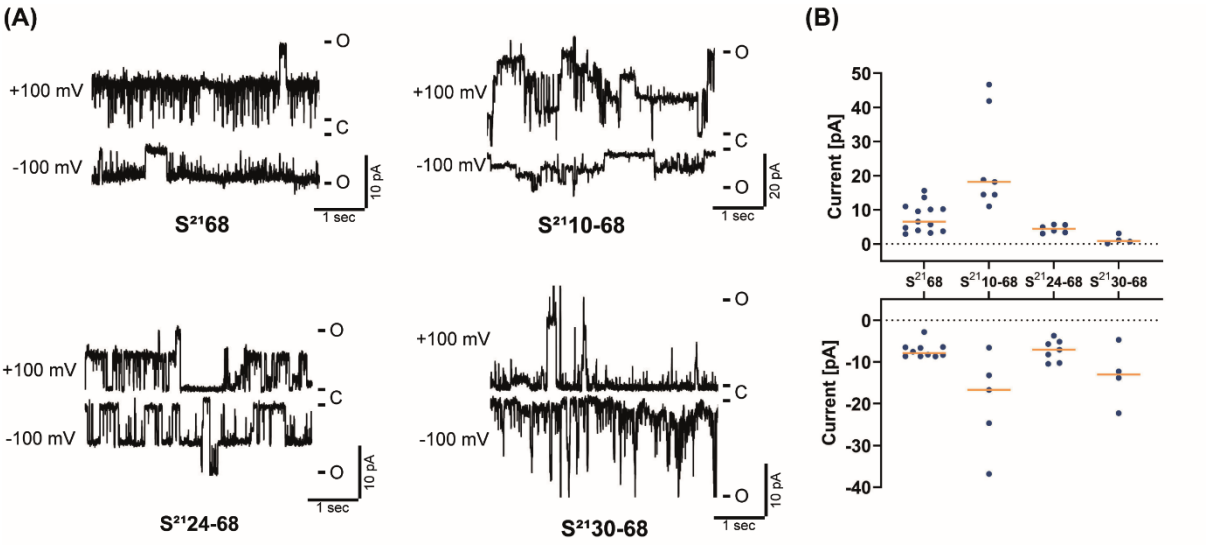

Fig. 7: Electrophysiological characterisation of the $S^{21}68$ holin and selected truncation mutants. **(A)** Summary of representative electrical recordings; The closed and open states are indicated as C and O; **(B)** The average current of individual truncation mutants correlates with the $T_{½}$ observed in the FuN Screen as $S^{21}10$-68 enables on average the greatest conductivity. The average current of a single 5 sec -100 mV or +100 mV protocol is indicated by a blue dot and orange lines mark the median.